Emission characteristics of quantum dots in planar microcavities

G. Ramon,[1,*] U. Mizrahi,[2] N. Akopian,[2] S. Braitbart,[2] D. Gershoni,[2] T. L. Reinecke,[1] B. D. Gerardot,[3] and P. M. Petroff[3]

[1]*Naval Research Laboratory, Washington, DC 20375-5320, USA*

[2]*The Physics Department and the Solid State Institute, Technion—Israel Institute of Technology, Haifa 32000, Israel*

[3]*Materials Department, University of California Santa Barbara, California 93106, USA*

(Received 14 November 2005; revised manuscript received 25 January 2006; published 17 May 2006)

The emission properties of single quantum dots in planar microcavities are studied experimentally and theoretically. Fivefold enhanced spontaneous emission outside the microcavity is found for dots in resonance with the cavity mode, relative to detuned dots. Using high-power excitation we obtain the in-plane cavity dispersion. Near-field images of the emission show spatial distributions of several micrometers for resonant dots, which decrease in size with the detuning from resonance. These experimental findings are explained using a simple and intuitive model.

I. INTRODUCTION

The potential applications of semiconductor quantum dots (QDs) as quantum light emitters have generated considerable research efforts in recent years.[1,2] Single-photon sources using quantum dots are an important ingredient in quantum information applications such as quantum cryptography and teleportation,[3] and may be further employed to implement efficient linear optics quantum computation[4] with the attainment of on-demand indistinguishable single-photon pulses,[5] and recently entangled photon pairs.[6] Single QDs can be excited either with continuous wave (cw), where they emit antibunched photons obeying a sub-Poissonian statistics, or with pulsed light, where a single photon, or correlated pairs are emitted per pulse.[1,2] It is the cascaded radiative recombination of electron-hole (*e-h*) pairs (or excitons) confined in single QDs that gives rise to the emission of single and correlated photons.

QD-based devices have several advantages as single-photon emitters. These include relatively large oscillator strengths, narrow spectral linewidths, and compatibility with mature semiconductor technologies. A major hindrance in their usefulness, though, is the low extraction efficiency of the emitted photons due to the high refraction index of the host semiconductor. Typically, only about 2% of the photons will be emitted from a GaAs-based device, while the rest will be lost due to total internal reflection. The general approach to overcome this problem has been to place the QDs at the antinode of a microcavity whose dimensions are comparable to the wavelength of the emitted photons.[7] In these cavities the number of allowed optical modes is reduced and at the same time, the in-cavity intensity of the allowed modes increases. As a result, the spontaneous recombination rate of excitons within these resonating modes is increased, a phenomenon known as the Purcell effect.[8,9]

Several approaches to realize three-dimensional (3D) photon confinement have been studied, including whispering-gallery modes in microdisks,[10] defect modes in 2D photonic crystals,[11] and lateral patterning of planar dielectric cavities using electron-beam lithography and etching.[9,12] The latter has proved particularly useful, demonstrating efficient pho-

ton emission in the weak-coupling regime,[9] and more recently strong coupling, paving the pathway for solid state realization of coherent control schemes.[12] In the strong-coupling regime, the interaction between the cavity mode and the emitter is larger than their combined decay rates, and the irreversible spontaneous emission from the QD exciton is replaced by a coherent exchange of energy between the exciton and the cavity mode. Among the challenges in the implementation of strong coupling in structured cavities, one notes the reduction in the cavity's *Q* factor due to the lateral patterning, and the lack of control in the in-plane positioning of the QD with respect to the lateral microstructure, resulting in a reduction in the oscillator strength of the confined exciton.[12,13]

In view of the technological difficulties associated with systems of QDs in 3D cavities, it seems important to study a system of QDs embedded in a planar microcavity, which is easier to fabricate. These cavities consist of distributed Bragg reflectors, which are typically stacks of alternating quarter-wavelength-thick layers of GaAs and AlAs, separated by a spacer layer of GaAs. Planar cavities can attain high *Q* factors due to the excellent control in their fabrication and embedding the QDs at the field's antinode is straightforward. These structures support an in-plane continuum of modes, and the interaction with QD excitons is therefore not expected to be in the strong-coupling regime.[14] Nevertheless, the spontaneous emission and the light extraction efficiency can still be enhanced considerably.[15] For example, a relatively weak planar cavity has been utilized recently to produce a tenfold increase in the efficiency of light collection of GaAs-based light-emitting diode structures.[16]

Unlike systems of quantum wells embedded in planar cavities, where polariton effects prevail and have been extensively studied (see, e.g., Refs. 17–20), QDs in planar cavities have received little attention.[21,22] Among the few experimental studies of this system, angle-resolved photoluminescence spectroscopy was used to detect TE-TM mode splitting (not to be confused with Rabi splitting, which is discernible only in the strong-coupling regime).[23]

In the present paper we study experimentally and theoretically single QD emitters in a planar microcavity. Using a partially covered layer of InGaAs self-assembled QDs placed

at the center of a λ microcavity, we have measured various characteristics of the spontaneous emission dynamics of the system such as spatial and angular distributions of the radiation field and its temporal decay. Our results are compared with a relatively simple theoretical analysis, which follows the treatment of Sugawara[21] and gives a simple and intuitive picture of the spontaneous emission properties of recombining excitons confined in QDs embedded in a planar microcavity. This approach accounts reasonably well for our experimental findings, including emission rates, radiative lifetimes, and angular and spatial distributions of the emission. In all of these measurements, a crucial parameter is found to be the detuning of the emitter energy from that of the cavity resonant mode. Since we do not have an exact knowledge of the QD size, shape, and composition, detuning from resonance is modeled in our approach either by varying the QD size or by varying its material band gap, while keeping the optical properties of the microcavity fixed.

The paper is organized as follows. In Sec. II we provide the details of our experimental system. Section III gives the theoretical model including the exciton wave functions and their interaction with the cavity field. In Sec. IV we give the experimental measurements and compare them with model calculations. A summary is given in Sec. V, and some details pertaining to the calculation of the excitonic wave function are given in the Appendix.

II. EXPERIMENTAL SETUP

The samples were grown by molecular-beam epitaxy on a (100)-oriented GaAs substrate. One layer of strain-induced InGaAs QDs was deposited in the center of a one-wavelength GaAs spacer layer. The height and composition of the QDs were controlled by partially covering the InAs QDs by a 30-Å-thick layer of GaAs and by subsequent 30 s growth interruption[24] to allow diffusion of In (Ga) atoms from (into) the strained islands. The growth resulted in $In_xGa_{1-x}As$ QDs whose estimated radius and composition are $150 \lesssim R_{QD} \lesssim 250$ Å and $0.47 \lesssim x \lesssim 0.53$, respectively, and height of 30 Å.

The sample was not rotated during the growth of the strained layer, resulting in a variable dot density across the sample's surface.[2] The estimated QD density in the sample areas that were measured is 10^8 cm^{-2}; however, the density of QDs that emit in resonance with the microcavity mode is more than two orders of magnitude lower. The GaAs spacer layer was grown to a width whose resonance mode matches the QD emission due to ground-state *e-h* pair recombinations (1λ cavity). The microcavity was formed by 25- and 11-period stacks of alternating quarter-wavelength layers of AlAs and GaAs below and above the spacer layer, respectively. The samples were not patterned or processed laterally to prevent obscuring the emission and its polarization.

For the optical measurements we used a diffraction-limited low-temperature confocal optical microscope.[33,34] The sample was cooled by a copper braid attached to the cold finger of a He-flow cryostat. The sample mount was accurately manipulated in three directions using computer-controlled motors. An X60 *in situ* microscope objective was

used in order to focus cw or pulsed laser light at normal incidence on the sample. The emitted light was collected by the same microscope objective. The collected light was spatially filtered, dispersed by a 0.22 m monochromator, and detected by a nitrogen-cooled charge-coupled device (CCD) array detector. The system provides diffraction-limited spatial resolution, in both the excitation and the detection channels. For the time-resolved spectroscopy, the dispersed light from the monochromator was focused onto a small, thermoelectrically cooled, single-channel avalanche silicon photodiode. The signal from the photodiode was analyzed using conventional photon-counting electronics. The photodiode dark count rate was 100 s^{-1}, and the system temporal resolution was approximately 250 ps.

III. THEORETICAL FRAMEWORK

The following approach assumes a single 1*s* exciton confined in a QD interacting with a discrete cavity mode. No charged exciton or biexciton states were considered, although their presence was confirmed in the measurements (see Sec. IV A). Our main interest in the current study is in the cavity effects on the exciton emission dynamics. The assumption of discrete cavity modes is justified for high-finesse cavities (we have verified that only the basic λ mode contributes appreciably to the interaction with the exciton). Although more complete description of the electromagnetic density of states in the cavity is available,[19] the main features of the exciton-photon coupling are well demonstrated within the framework of our simplified model.

A. Model wave function for quantum dot excitons

We start by solving for the excitonic wave function in a quantum dot, considering a finite potential barrier in the growth (*z*) direction and a parabolic potential in the lateral direction.

The effective mass Hamiltonian is given by

$$H = -\frac{\hbar^2}{2m_e^{\parallel}}[\nabla_{\rho_e}^2 + \sigma\nabla_{\rho_h}^2 + \sigma_{ez}\partial_{z_e}^2 + \sigma_{hz}\partial_{z_h}^2]$$
$$- \frac{e^2}{\epsilon\sqrt{(\boldsymbol{\rho}_e - \boldsymbol{\rho}_h)^2 + (z_e - z_h)^2}} + V_e(\boldsymbol{\rho}_e, z_e) + V_h(\boldsymbol{\rho}_h, z_h),$$
$$(1)$$

where $\mathbf{r}_i = (\boldsymbol{\rho}_i, z_i)$ are the electron or hole in-plane and *z* coordinates, and $\sigma = m_e^{\parallel}/m_h^{\parallel}$, $\sigma_{ez} = m_e^{\parallel}/m_e^z$, and $\sigma_{hz} = m_e^{\parallel}/m_h^z$ are the appropriate effective mass ratios in the plane and *z* directions, and ϵ is the background dielectric constant screening the Coulomb interaction. In Eq. (1) we have neglected the differences in the conduction- and valence-band masses and in the dielectric constant value of the two semiconductors that comprise the QD and its host. In the case of strong *z*-direction confinement, the electron and hole potentials can be approximated as

$$V_i(\boldsymbol{\rho}_i, z_i) \approx V_i(\boldsymbol{\rho}_i) + V_i(z_i), \quad i = e, h \qquad (2)$$

thus decoupling the problem into lateral and *z* parts, and enabling us to write the envelope wave function for the exciton in the form

$$\Phi_x(\mathbf{r}_e, \mathbf{r}_h) = \Psi_x(\boldsymbol{\rho}_e, \boldsymbol{\rho}_h)\chi_e(z_e)\chi_h(z_h) \tag{3}$$

(for infinite z-direction potential, this approximation is exact). Transforming to center of mass (c.m.) and relative in-plane coordinates,

$$\mathbf{R} = \frac{\sigma\boldsymbol{\rho}_e + \boldsymbol{\rho}_h}{1 + \sigma}, \quad \mathbf{r} = \boldsymbol{\rho}_e - \boldsymbol{\rho}_h, \tag{4}$$

we separate the c.m. motion and relative-motion wave functions, $\Psi_x(\mathbf{R}, \mathbf{r}) = \psi(\mathbf{R})\phi(\mathbf{r})$, by choosing parabolic potentials for the lateral confinement of both electron and hole:[25,26]

$$V_i(\boldsymbol{\rho}_i) = \frac{1}{2}m_i^{\parallel}\omega^2\rho_i^2, \quad i = e, h. \tag{5}$$

Employing natural units of length and energy, namely, the bulk effective Bohr radius ($a_B = \hbar^2\epsilon/m_e^{\parallel}e^2$) and Rydberg ($\mathrm{Ry} = \hbar^2/2m_e^{\parallel}a_B^2$), the Hamiltonian in Eq. (1) takes the form

$$H = H_R + H_r,$$

$$H_R = -\frac{\sigma}{1 + \sigma}\nabla_R^2 + \frac{4\sigma R^2}{\xi^4(1 + \sigma)},$$

$$H_r = -[(1 + \sigma)\nabla_r^2 + \sigma_{ez}\partial_{z_e}^2 + \sigma_{hz}\partial_{z_h}^2] - \frac{2}{\sqrt{r^2 + (z_e - z_h)^2}}$$

$$+ \frac{4\sigma^2 r^2}{\xi^4(1 + \sigma)^3} + V_e(z_e) + V_h(z_h) \tag{6}$$

where ξ is a dimensionless lateral localization parameter related to the confining potential by

$$\xi = \frac{1}{a_B}\sqrt{\frac{2\hbar}{M_x\omega}} \tag{7}$$

and $M_x = m_e^{\parallel} + m_h^{\parallel}$ is the in-plane c.m. exciton mass.

We identify the in-plane c.m. motion part with a 2D harmonic oscillator Hamiltonian, which is solved analytically resulting in wave functions $\psi(\mathbf{R})$ that are given by the associated Laguerre polynomials.[27] In what follows, we will be interested only in the c.m. motion ground state which is a 2D Gaussian function. By equating the areal size of the c.m. wave functions with the physical QD radius: $|\int\psi(\mathbf{R})d^2R|^2 = 2\pi\xi^2 = \pi R_D^2$, we relate the potentials (5) to the QD size.

For the in-plane relative coordinates we employ a trial wave function[27]

$$\phi(r) = \mathcal{N}_r e^{-(r/\eta)^{\alpha}} \tag{8}$$

where $\mathcal{N}_r$ is a normalization constant and η, α are variational parameters. α has values between 1 (no lateral confinement—very large QDs) and 2 (strong lateral confinement—very small QDs). Considering finite-height potentials in the z direction, $V_i(z_i) = V_i^z\Theta(|z_i| - L/2)$ where $i = e, h$ and L is the QD height, we have for the z wave functions[28,29]

$$\chi_i(z_i) = \mathcal{N}_{z_i} \times \begin{cases} \cos(k_i z_i), & |z_i| \leq L/2, \\ \dfrac{k_i}{\sqrt{k_i^2 + \kappa_i^2}}e^{-\kappa_i(|z_i| - L/2)}, & |z_i| > L/2, \end{cases} \tag{9}$$

where $i = e, h$, $\mathcal{N}_{z_i} = (L/2 + 1/\kappa_i)^{-1/2}$ is a normalization constant,

$$k_i = \sqrt{\frac{2m_i^z}{\hbar^2}E_{i0}^z}, \quad \kappa_i = \sqrt{\frac{2m_i^z}{\hbar^2}(V_i^z - E_{i0}^z)}, \tag{10}$$

and E_{i0}^z is determined by the ground-state quantization condition

$$\sqrt{\frac{E_{i0}^z}{V_i^z}} = \cos\left(\frac{L}{2}\sqrt{\frac{2m_i^z}{\hbar^2}E_{i0}^z}\right). \tag{11}$$

The variational parameters in Eq. (8) are calculated by maximizing the magnitude of the ground-state exciton binding energy $E_B = E_{e0}^z + E_{h0}^z + E_{1s}^{\text{c.m.}} - E_r$, where $E_{1s}^{\text{c.m.}} = \hbar\omega = \frac{4\sigma}{\xi^2(1 + \sigma)}$ is the ground-state energy of the c.m. motion and E_r is the expectation value of the relative motion part of the Hamiltonian in Eq. (6) (see the Appendix).

The InGaAs self-assembled QDs that we are considering have an estimated height of $L = 30$ Å. The conduction- and valence-band in-plane and normal-to-the-plane masses were calculated for $L = 30$ Å, assuming 50% InAs content, using an eight-band Kane model, and taking into account both non-parabolicity and lattice-mismatch strain effects.[30] We find for the electron $m_e^{\parallel} = 0.0630$, $m_e^z = 0.0897m$, and for the heavy hole $m_h^{\parallel} = 0.1573m$, $m_h^z = 0.3406m$. For the potential barriers we find $V_e^z = 441.9$ meV and $V_h^z = 110.6$ meV. Using these values we minimize Eq. (A1) with respect to the two variational parameters α and η, and find the binding energy of the ground-state heavy-hole exciton as a function of the QD radius shown in Fig. 1.

B. Exciton-photon interaction in a planar microcavity

In the following we assume weak coupling between the QD exciton and the cavity modes. This is justified *a posteriori* by the calculated spontaneous emission linewidths, which are always much smaller than that of the cavity. The cavity photon escape rate was deduced from the measured reflectivity of the cavity. We have put the cavity structure into a linear dispersion model and calculated its reflectivity using transfer matrix formalism. The resulting cavity mode linewidth was close to the measured value.

The interaction between an exciton and the electromagnetic field is given by

$$H_{int} = -\frac{e}{mc}\sum_{\mathbf{k},\sigma}\mathbf{p}\cdot\mathbf{A}_{\mathbf{k}}^{\sigma} \tag{12}$$

where $\mathbf{A}_{\mathbf{k}}^{\sigma}$ is the vector potential associated with the kth mode with polarization σ and we have neglected the quadratic term in $\mathbf{A}$. In a planar cavity, with z in the growth direction, the Maxwell equations with the appropriate boundary conditions yield two solutions for the electromagnetic field.[31] These correspond to the electric vector being normal to (TE) or in
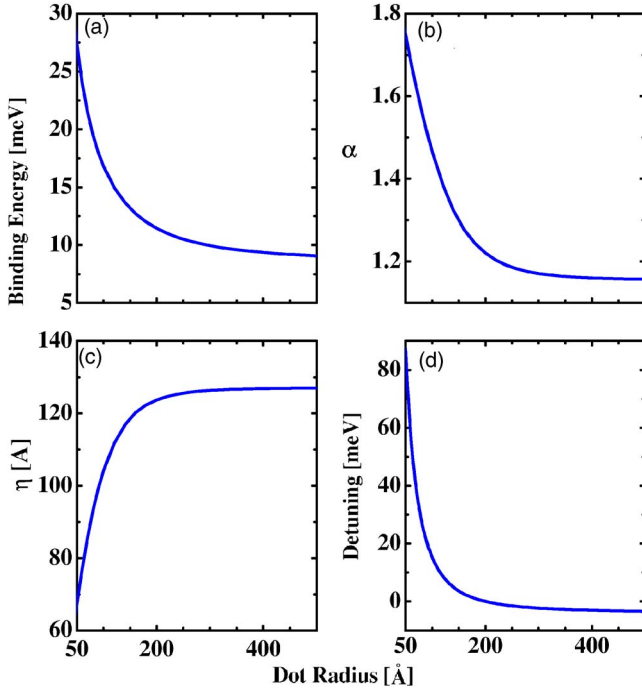
FIG. 1. (Color online) (a) Exciton binding energy, (b) variational parameter α, (c) variational parameter η, and (d) detuning of the exciton line with respect to the cavity mode, as functions of the QD radius (resonance was assumed for $R_D = 200$ Å).

(TM) the plane defined by the wave vector $\mathbf{k} = (\mathbf{k}_\parallel, k_z)$ and z, and are given (using the Coulomb gauge) by

$$\mathbf{A}_\mathbf{k}^{\mathrm{TE}} = -i\sqrt{\frac{2\pi\hbar v}{kV_c}}\cos(k_z z)\mathbf{e}_\parallel(e^{i\mathbf{k}_\parallel\cdot\boldsymbol{\rho}}\hat{a}_\mathbf{k} + e^{-i\mathbf{k}_\parallel\cdot\boldsymbol{\rho}}\hat{a}_\mathbf{k}^\dagger),$$

(13a)

$$\mathbf{A}_\mathbf{k}^{\mathrm{TM}} = \sqrt{\frac{2\pi\hbar v}{kV_c}}\left(-i\frac{k_z}{k}\cos(k_z z)\mathbf{e}_\parallel + \frac{k_\parallel}{k}\sin(k_z z)\mathbf{e}_\perp\right)$$
$$\times (e^{i\mathbf{k}_\parallel\cdot\boldsymbol{\rho}}\hat{a}_\mathbf{k} + e^{-i\mathbf{k}_\parallel\cdot\boldsymbol{\rho}}\hat{a}_\mathbf{k}^\dagger)$$

(13b)

where $v = c/n_{eff}$ is the velocity of light in the cavity medium, V_c is the cavity quantization volume, and $\hat{a}_\mathbf{k}^\dagger$ ($\hat{a}_\mathbf{k}$) is the creation (annihilation) operator of the $\mathbf{k}$ field mode. In Eqs. (13) k_z satisfies the resonance condition

$$k_z = \frac{2m\pi}{L_c},$$

(14)

where m takes any integer value and L_c is the cavity width. Here we have considered only even modes which are the only ones that couple with the exciton ground state.[18] Assuming a system of a single exciton and a single photon, appropriate for low exciton densities, the time-dependent state of the system is given by

$$|\Psi(t)\rangle = b(t)e^{-i\omega_x t}|\Phi_x, 0\rangle + \sum_{\mathbf{k},\sigma} c_{\mathbf{k},\sigma}(t)e^{-i\omega_k t}|\Phi_g, 1_{\mathbf{k},\sigma}\rangle$$

(15)

where ω_x (ω_k) is the exciton (electromagnetic field) resonant frequency, and σ runs over the two light polarizations. Taking the system to be initially with one exciton and the radiation field in the vacuum state [$b(0)=1$, $c_{\mathbf{k},\sigma}(0)=0$] we write the equations of motion for $b(t)$ and $c_{\mathbf{k},\sigma}(t)$, using the rotating-wave approximation:

$$\dot{b}(t) = -i\sum_{\mathbf{k},\sigma} g_{\mathbf{k},\sigma}e^{i(\omega_x - \omega_k)t}c_{\mathbf{k},\sigma}(t) - \frac{\gamma_x}{2}b(t),$$

(16a)

$$\dot{c}_{\mathbf{k},\sigma}(t) = -ig_{\mathbf{k},\sigma}^* e^{-i(\omega_x - \omega_k)t}b(t) - \frac{\gamma_c}{2}c_{\mathbf{k},\sigma}(t).$$

(16b)

In Eqs. (16) γ_x is the exciton broadening due to all processes other than spontaneous emission (phonon scattering, nondiative recombination), and γ_c is the decay rate of the cavity photon mode due to mirror losses, which is inversely proportional to the cavity quality factor. The exciton-photon coupling constant appearing in Eqs. (16) is given by

$$\hbar g_{\mathbf{k},\sigma} = -\langle\Phi_x, 0|\frac{e}{mc}\mathbf{p}\cdot\mathbf{A}_\mathbf{k}^\sigma|\Phi_g, 1_{\mathbf{k},\sigma}\rangle.$$

(17)

The coupling constant is related to the total oscillator strength per unit area $f_\mathbf{k}$ through

$$\sum_{\sigma=\mathrm{TE,TM}} |g_{\mathbf{k},\sigma}|^2 = \frac{2\pi e^2\omega_x}{n_{eff}mckL_c}f_\mathbf{k}.$$

(18)

Using the dipole approximation ($\mathbf{k}_e \approx -\mathbf{k}_h$), considering both polarizations, and neglecting intersubband mixing, $f_\mathbf{k}$ is calculated to be

$$f_\mathbf{k} = |\widetilde{\psi}(k_\parallel)|^2\left[\left(1 + \frac{k_z^2}{k^2}\right)\cos^2(k_z z)f_\parallel + \frac{k_\parallel^2}{k^2}\sin^2(k_z z)f_\perp\right]$$

(19)

where

$$f_\parallel = \frac{|\phi(0)|^2}{m\hbar\omega_x}|P_{cv}F_{\mathbf{e}_\parallel}|^2|\langle\chi_e|\chi_h\rangle|^2,$$

(20a)

$$f_\perp = \frac{|\phi(0)|^2}{m\hbar\omega_x}|P_{cv}F_{\mathbf{e}_\perp}|^2|\langle\chi_e|\chi_h\rangle|^2.$$

(20b)

In Eqs. (19) and (20) $\widetilde{\psi}(k_\parallel)$ is the in-plane Fourier-transformed exciton c.m. wave function, $\phi(0)$ is the in-plane exciton relative motion wave function at zero, P_{cv} is the bulk transition matrix element, and $F_{\mathbf{e}_\parallel}$ ($F_{\mathbf{e}_\perp}$) is the parallel (perpendicular) polarization factor in quantum wells.[27]

We note that the coupling constant in planar cavities is determined by $f_\mathbf{k}/L_c$, as opposed to 3D cavities where the relevant quantity is f/V_m, where f is the oscillator strength and V_m is the cavity mode volume. The main difference in the oscillator strength for quantum well (QW) excitons versus that for QD excitons is due to the localization of the c.m.

wave function of the latter [see Eq. (19)]. Since only excitons with in-plane wave vectors smaller than $q_x = \omega_x/v$ can radiate spontaneously due to the resonance condition, the spread in the **k**-space c.m. wave function for QD excitons results in a smaller effective oscillator strength, accounting for their observed increased spontaneous emission lifetimes, as compared with QW excitons.

Integrating Eq. (16b) and substituting the resulting $c_{\mathbf{k},\sigma}(t)$ in Eq. (16a) we have the integro-differential equation

$$\dot{b}(t) = -\sum_{\mathbf{k},\sigma} |g_{\mathbf{k},\sigma}|^2 \int_0^t d\tau\, b(\tau) e^{[-i(\omega_{\mathbf{k}}-\omega_x)-\gamma_c/2](t-\tau)} - \frac{\gamma_x}{2} b(t).$$

(21)

In the weak-coupling regime, which is clearly our case, $\gamma_c \gg g$ and one can solve Eq. (21) to a good approximation by taking $b(t)$ out of the integral. For $t \gg \gamma_c^{-1}$ the result is

$$\dot{b}(t) = -\frac{\gamma_x + \gamma_{SE}}{2} b(t)$$

(22)

where

$$\gamma_{SE} = 2\pi \sum_{\mathbf{k},\sigma}{}' |g_{\mathbf{k},\sigma}|^2 \mathcal{L}(\omega_{\mathbf{k}} - \omega_x, \gamma_c)$$

$$= \frac{4\pi^2 e^2 \omega_x}{n_{eff}^2 m L_c} \sum_{\mathbf{k}}{}' \frac{f_{\mathbf{k}}}{\omega_{\mathbf{k}}} \mathcal{L}(\omega_{\mathbf{k}} - \omega_x, \gamma_c),$$

(23)

and

$$\mathcal{L}(\omega_{\mathbf{k}} - \omega_x, \gamma_c) = \frac{1}{2\pi} \frac{\gamma_c}{(\omega_{\mathbf{k}} - \omega_x)^2 + (\gamma_c/2)^2}$$

(24)

is the normalized Lorentzian cavity-mode broadening. The prime over the sum in Eq. (23) indicates taking the lowest cavity mode, $k_z = 2\pi/L_c$, and summing over the in-plane photon wave vectors, $\mathbf{k}_\parallel \le q_x$, where $q_x = \omega_x/v$ is the maximum exciton in-plane wave vector that can still couple to the cavity mode resulting in radiative recombination of the exciton. The solution of Eq. (22) gives an exponential irreversible spontaneous emission of the exciton due to its coupling with the cavity field modes, representing Fermi's golden rule. As long as the calculated γ_{SE} is much smaller than the cavity broadening γ_c, the weak-coupling approximation holds; otherwise, one must solve the general equation (21).

IV. RESULTS

We are interested in particular in the influence of the cavity on the exciton's spontaneous emission, radiative lifetime, and emission distribution.

A. Exciton spontaneous emission

Figure 2 shows the measured reflectivity of the cavity and the integrated photoluminescence intensity, using relatively high-power, constant excitation. The same setup was used to measure both the reflectivity and the photoluminescence. Each point in the figure results from emission from a distinct QD. For the reflectivity measurements, white light from a
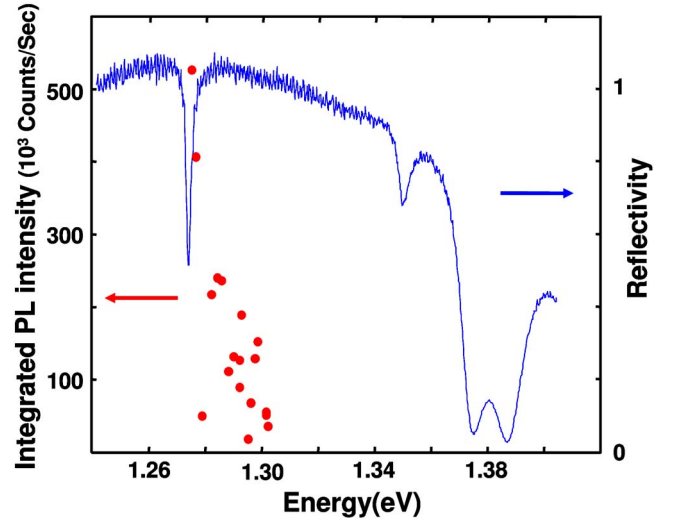

FIG. 2. (Color online) Measured reflectivity [(blue) line] and integrated photoluminescence intensity [(red) points] of QDs at the antinode of a planar λ cavity.

tungsten lamp was reflected from the sample, dispersed by the monochromator and detected by the CCD camera. The measured reflectivity spectrum was then normalized by the reflectivity of a front-surface aluminum mirror. The numerical aperture of our microscope objective in the photoluminescence (PL) measurements was 0.8, resulting in a collection angle of $\sim 13.2°$ inside the sample. The figure shows a sharp dip in the reflectivity corresponding to the resonant cavity mode. The full width at half maximum is 1.94 meV giving a Q factor of 670. The emission intensity shows a pronounced enhancement for QDs in resonance with the cavity mode. A rapid decrease in the emission intensity to a value roughly five times smaller is found for QDs detuned by 20–25 meV. Emission from negatively detuned QDs is largely inhibited due to the resonance condition, and no spectral emission is observed below the cavity mode energy.

In order to discuss these data, we relate the detuned exciton line to the λ cavity width by[21]

$$L_c = \frac{\lambda_x}{n_{eff}} \zeta = \frac{2\pi}{q_x} \zeta,$$

(25)

where ζ corresponds to the detuning of the exciton line from resonance. We assume the cavity resonant mode matches the emission from the heavy-hole $1s$ exciton of a QD with a radius $R_D = 200$ Å, for which $\zeta = 1$. The corresponding resonance energy is calculated using Eq. (A1) to be $E_x^{res} = E_c = 1.2756$ eV. In order to model microscopically the emission from quantum dots that are detuned from this resonance, we represent the detuning by either changing the QD size or by changing the QD material band gap (via the dot composition). The dependence of the detuning on the QD radius is given in Fig. 1(d). Considering only the basic cavity mode expressed as $k_z = q_x/\zeta$, Eqs. (23) and (19) are used to give
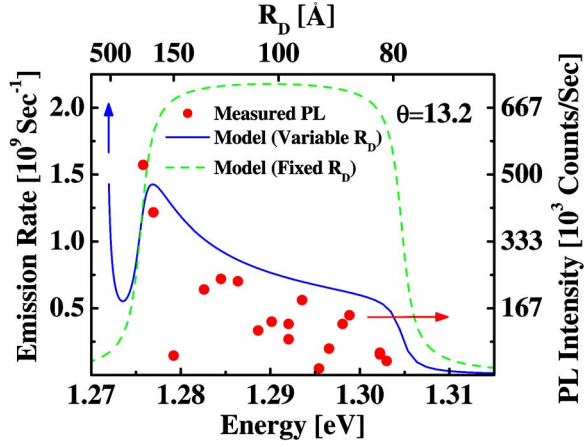
FIG. 3. (Color online) Emission rates into a collection angle 13.2° vs exciton energy. Full (red) circles are the measured values given in counts per second (right axis). Solid (blue) line shows the calculation where detuning is obtained by varying the QD radius (given in the top axis). Dashed (green) line shows the calculation with QD size fixed to $R_D=200$ Å and the detuning obtained by varying the QD material band gap. A scaling factor of 3000 was taken between the left and right axes (see text).

$$\gamma_{SE} = \frac{\pi e^2 \omega_x^2 R_D^2 f_{\parallel}}{mc^2 \zeta} \int_0^{q_x} dq \, q e^{-R_D^2 q^2/4} \frac{q^2 + 2q_x^2/\zeta^2}{(q^2 + q_x^2/\zeta^2)^{3/2}}$$
$$\times \mathcal{L}(v\sqrt{q^2 + q_x^2/\zeta^2} - \omega_x, \gamma_c). \quad (26)$$

In deriving Eq. (26) we assumed that the QD resides in the center of the cavity, where the cavity mode takes its maximum value, and considered only the heavy-hole exciton whose perpendicular transition matrix element vanishes, $f_{\perp}=0$. To account for the experimental collection angle, the upper limit of the integration in Eq. (26) is replaced with $q_0=q_x \sin \theta$, where θ is measured from the z axis.

In the calculation we used $n_{eff}=3.5$, $\epsilon=13.9$, resulting in a QW exciton Bohr radius of $a_B=116.7$ Å. The free (QW) exciton oscillator strength per unit area was calculated for a 30 Å $In_{0.53}Ga_{0.47}As$ QW and was found to be $f_{\parallel}=7.1 \times 10^{-5}$ Å^{-2}.[27,32] This value increases as the QD size reduces, due to the shrinkage of the relative motion wave function [see Eqs. (20)]. We stress that this effect is overshadowed by the spread in the c.m. $\mathbf{k}$-space wave function as the QD size reduces; therefore $f_{\mathbf{k}}$ will still decrease for smaller QDs. We took an additional factor of 2 for the oscillator strength to account for the two-spin configurations.

In Fig. 3 the calculated exciton spontaneous emission rates are shown together with the measured PL values as functions of exciton energy. The solid (blue) line corresponds to a calculation where detuning of the exciton energy was obtained by varying the QD radius whereas for the dashed (green) line the QD size was fixed to $R_D=200$ Å and its band gap was varied. In order to put the measured and calculated values on the same figure, a scaling factor of 3000 was taken between the right (photon counts) and left (emission rate) axes. This factor corresponds to the photon extraction efficiency in the experiment, which was estimated from pulsed excitation measurements.[33]
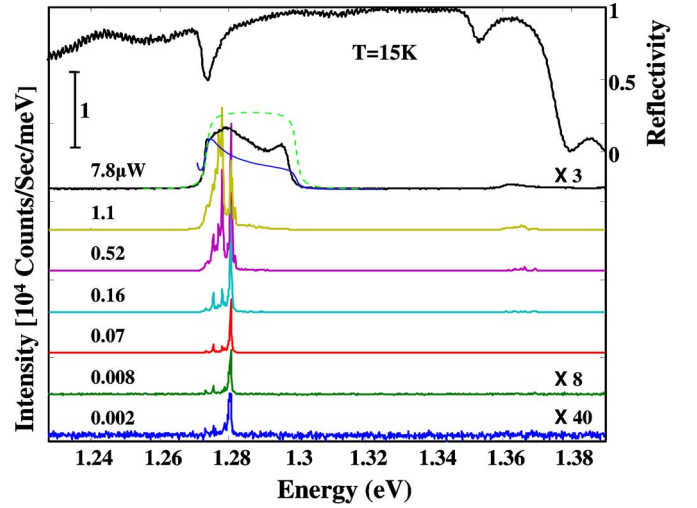

FIG. 4. (Color online) Measured reflectivity (upper line) and integrated PL intensity for various excitation powers. Calculated emission rates with detuning by varying the QD radius [solid (blue) line] and its material band gap [dashed (green) line] are superimposed on the measured PL with the highest excitation power.

The calculated results obtained by varying the dot size agree qualitatively with the experimental data, including the rapid falloff in the PL intensity away from resonance. The range of $90 \lesssim R_D \lesssim 300$ Å that accounts for a detuning range of ~20 meV is consistent with variations in typical self-assembled InGaAs QDs. The two model calculations in Fig. 3 show marked differences. In particular, the emission enhancement shown for negative detuning in the case of variable QD size is missing in the fixed-QD-size calculation. The latter case shows a rapid inhibition of the emission as the QD becomes negatively detuned out of the cavity mode linewidth, which is clearly a cavity effect. In the case of variable R_D the cavity effect competes with the localization of the exciton c.m. wave function in $\mathbf{k}_{\parallel}$ space, as the QD size increases [Eq. (26)]. This effect is consistent with the strong increase in QD exciton lifetime as compared with QW excitons. The competition between the cavity and localization effects is shown in the figure by the dip in the calculated emission rate (solid line) for $R_D \sim 300$ Å (negative detuning). For yet larger QDs the localization effect takes over and the emission rate rapidly increases (the figure includes QDs with $R_D \lesssim 600$ Å). Such large QDs are less likely to form in our case and this increase is therefore not observed.

Figure 4 shows the dependence of the QD spontaneous emission on the excitation power. At low excitation the PL is dominated by a sharp emission line arising from the recombination of the $1s$ exciton. As the excitation power is increased, the dot is populated with more carriers and recombinations of multiexcitons from higher collective states appear in the spectrum.[33,34] For still higher excitation powers the emission is broadened and is extended beyond the cavity mode linewidth (see the reflectivity curve in Fig. 4). This is qualitatively confirmed by calculated emission rates that are superimposed over the high-excitation-power PL curve (topmost PL spectrum in Fig. 4). As before, the detuning of higher dot states is represented by varying either the dot size
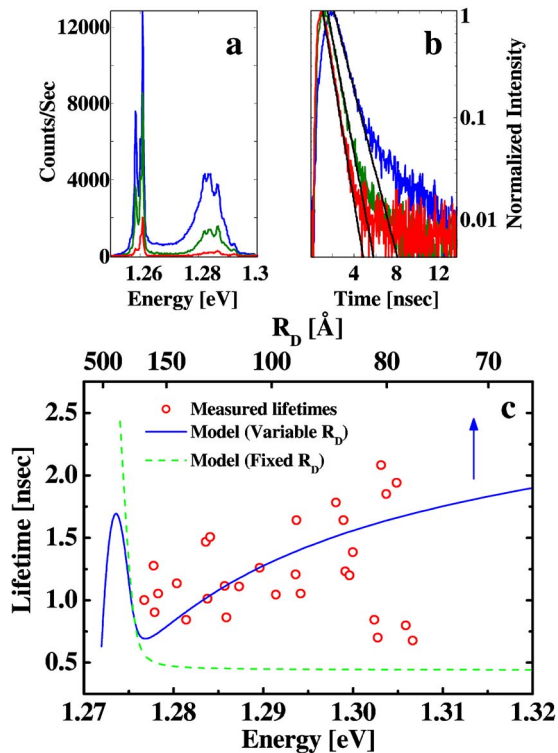
FIG. 5. (Color online) (a) Photoluminescence spectra of a single QD for various excitation intensities; (b) corresponding decay time measurements. The fitted monoexponential decay models are indicated by the black lines. The green curve (obtained at excitation power of 0.5 mW) was measured under saturation conditions and was used for the measured PL decay time. (c) Exciton radiative lifetime vs its energy. Open (red) circles are the measured values. Solid (blue) line shows the calculation where detuning is obtained with variable QD radius (given in the top axis). Dashed (green) line shows the calculation with QD size fixed to $R_D = 200$ Å and its band gap varied.

[solid (blue) line] or its material band gap [dashed (green) line].

In Fig. 5(c) we plot the experimental and calculated exciton lifetimes as functions of the emission spectral energy. Each point in the figure represents a measurement from a specific QD (open circles). The sample temperature during the measurements was 15 K. The emission lifetime was estimated from a single-exponential fit to the initial part of the measured PL decay curves [(black) lines in Fig. 5(b)]. In general, the decay curves were quite sensitive to the excitation intensity and they were not single exponentials, as can be seen in Fig. 5(b). For the measurements we used excitation intensities which exactly saturate the PL emission [(green) curve in Figs. 5(a) and 5(b)]. We note that there is a considerable scatter in the measured data. We believe that this scatter is mainly due to nonradiative processes, which may depend on the particular environment and charge state of a given QD. Also, as mentioned above, the measured decay times were excitation intensity dependent. Our particular choice of excitation intensity, for which the exciton PL saturates, may be somewhat arbitrary. The saturation excitation may vary from one QD to the other in a way that has little to do with the microcavity.
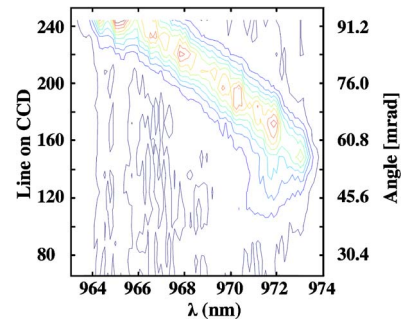

FIG. 6. (Color online) Contour plot of the PL intensity from a highly excited single resonant QD in a planar microcavity as a function of photon wavelength and emission angle. Each contour represents 10% of the maximal intensity.

For the model in which the detuning is represented by varying the QD material band gap (dashed line), above resonance there are always cavity modes in the 2D continuum that can couple to the exciton due to the photon in-plane dispersion; thus the coupling remains effective even for a large positive detuning, resulting in a short recombination time. The emission from negatively detuned QDs is largely inhibited consistent with the experiment where emission from these QDs is not observed. This inhibition depends strongly on the cavity Q factor and would be much less pronounced for weaker cavities. The calculations in which detunings are represented by varying the dot size (solid line) show a different behavior. When the QD radius is reduced (energies above resonance in Fig. 5) the lifetime increases due to the spread of the exciton c.m. wave function in $k_\parallel$ space, as explained above. The very different lifetime behavior of the two detuning mechanisms may aid in identifying the various QDs. The results of both Figs. 3 and 5 seem to indicate that the majority of QDs have similar composition and their variations are mainly in size.

We note that the increase in radiative lifetime with reduction of the QD size is suppressed in the limit of strong confinement. This is because the oscillator strength ($f_\parallel$) increases due to the localization of the relative motion wave function. This effect is superseded by the breakdown of the selection rule caused by the spread of the c.m. **k**-space wave function outside q_x. Also note that the calculated linewidths due to spontaneous emission are at most $\gamma_{SE} \lesssim 1.6$ μeV $\ll \gamma_c$; thus, we are always in the weak-coupling regime where our approximate solution is valid.

Next, angle-resolved spectroscopy was performed on a single QD using high-power excitation (8 μW). In these conditions the QD is populated with many carriers resulting in many available recombination channels. The PL spectrum therefore reflects the density of electromagnetic modes in the cavity. Figure 6 shows a contour plot giving the measured PL intensity of a highly excited single QD, as registered by the CCD array camera at the exit of the monochromator. The horizontal axis gives the spectral dispersion while the vertical axis gives the angular distribution. Since the k_z part of the emission is fixed by the resonance condition to the cavity mode, this angle corresponds to the in-plane wave vector of the emission. From the geometry and lenses used for the
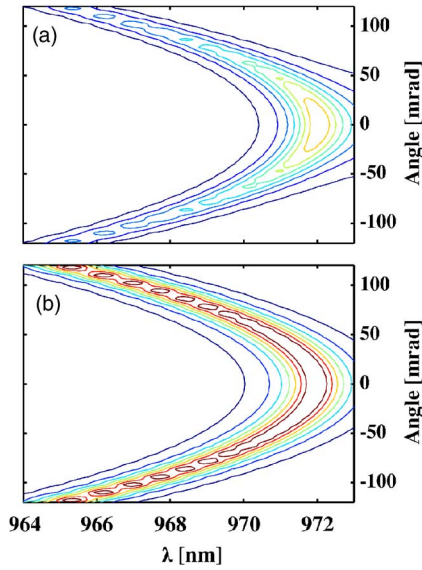
FIG. 7. (Color online) Contour plot of the calculated emission rate distributions as a function of photon wavelength and emission angle ($\mathbf{k}_\parallel$). Each contour represents 10% of the maximal rate. Detuning is obtained by (a) varying the QD radius, and (b) varying the QD material band gap and fixing the dot radius to $R_D = 200$ Å.

imaging we estimate that each row in the CCD camera is equivalent to 0.38 mrad. The figure clearly demonstrates the in-plane dispersion of the cavity mode. The peaks in the emission intensity shown in the figure are most likely related to recombinations from various carrier configurations, e.g., the neutral and charged excitons, biexcitons, and higher-order multiexcitons,[33,34] of the single QD. These multiexciton lines appear due to the high excitation power used in this experiment. Since our model accounts only for the neutral exciton line, we cannot compare our experimental data directly with the model calculations. Nevertheless, by taking the derivative of Eq. (26) with respect to the $\mathbf{k}_\parallel$ space area (using $q = q_x \sin \theta$), we can achieve a similar in-plane dispersion of the cavity mode, as shown in Fig. 7. The models of QDs in which the size and the material band gap were varied to represent the detuning show similar dispersion behavior. The difference between the two cases is mainly that in the case of fixed QD size the emission extends over a larger energy range [Fig. 7(b)], which can be explained using the preceding arguments. We attribute the difference between the symmetric shape of the calculated angle-resolved spectrum and the asymmetric shape of the measured one to the finite aperture of the confocal setup. The data were taken from a single QD that was positively detuned with respect to the microcavity resonance. Due to the relatively large spatial distribution of the emission from the QD (see Sec. IV B), we could not collect the light from both negative and positive emission angles.

B. Spatial distribution of the emission

We now turn to examine the in-plane spatial spread of a single QD emission. Figure 8(a) shows a spatially integrated emission spectrum from a particular QD under moderate ex-
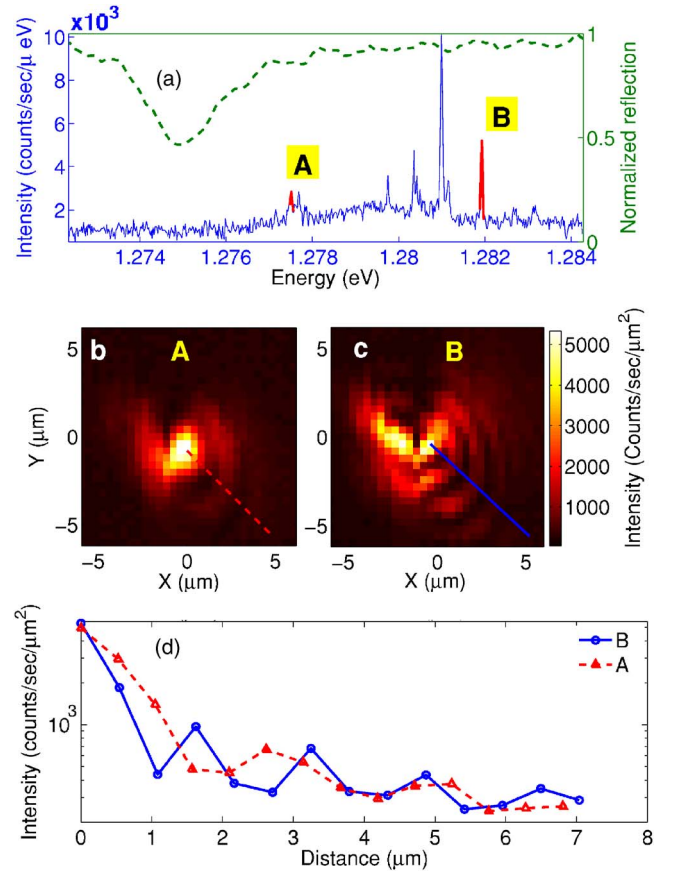

FIG. 8. (Color online) (a) Spatially integrated emission spectrum measured from a single QD under moderate excitation power. The dashed (green) line shows the normalized reflection of the sample. Wavelength-selective spatial image measured for (b) spectral line *A* and (c) spectral line *B*. (d) Emission intensities along the diagonals which are marked by dashed (red) and solid (blue) lines as functions of the distance from the image center.

citation power. Few discrete spectral lines are observed. Each spectral line corresponds to a particular emission line arising from the recombination of a ground-state *e-h* pair from different many-carrier collective states.[34] For our purpose it suffices to note that each line is spectrally detuned differently from the cavity mode. In order to estimate the spectral detuning of each line the reflectivity spectrum from this sample is overlaid on the emission spectrum in Fig. 8(a). The least- and most-detuned lines are marked in the figure by *A* and *B*, respectively. Wavelength-selective spatial images of the least- (*A*) and most- (*B*) detuned spectral lines are shown in Figs. 8(b) and 8(c), respectively. The intensity distributions of the electromagnetic fields associated with the emission lines are essentially symmetric, though some obscuration, which can be partially attributed to mechanical drift, is present. The emission patterns contain a central strong spot surrounded by concentric rings with decreasing intensities. The intensities along the diagonals, which are marked by dashed (red) and solid (blue) lines in Figs. 8(b) and 8(c), respectively, are displayed as functions of the in-plane distance from the image center in Fig. 8(d).

Figures 9(a) and 9(b) show the calculated images for the detunings of lines *A* and *B*, respectively. Since both spectral
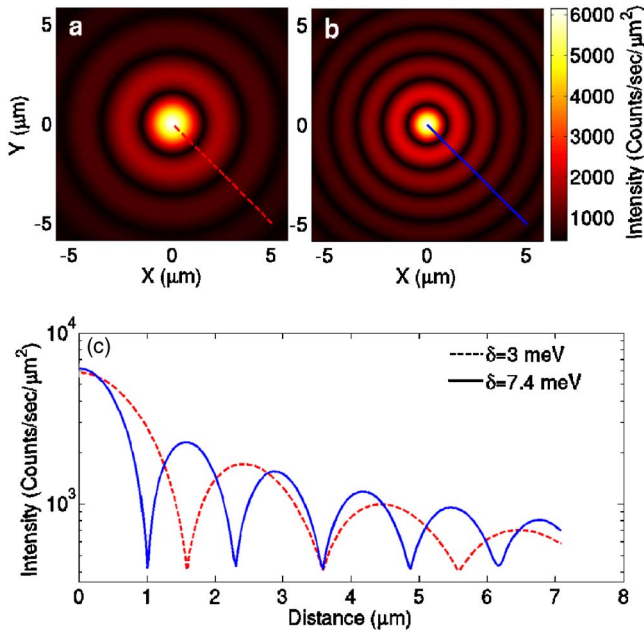
FIG. 9. (Color online) Calculated spatial spread of the emission from a single QD detuned from resonance by $\delta=$ (a) 3, (b) 7.4 meV, corresponding to the measured spectral lines marked *A* and *B* in Fig. 8, respectively. Detuning is modeled by varying the QD material band gap while the QD radius is fixed to $R_D = 200$ Å. (c) Calculated emission intensities as functions of the distance from the image center. (Constant background of 400 counts was added to the calculated emission to facilitate comparison with the measured data.)
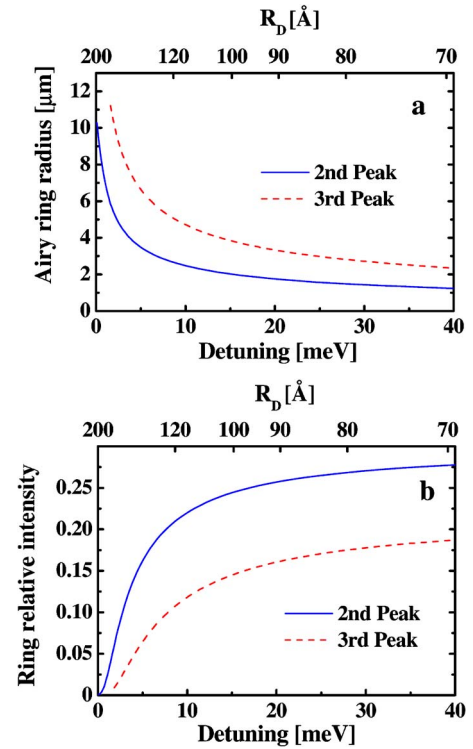

FIG. 10. (Color online) (a) Calculated positions of second and third rings in the emission distribution; (b) calculated emission intensity of second and third rings normalized to central emission peak.

lines originate from the same QD, we used different band gaps to obtain the detuning. The images were generated by calculating the in-plane Fourier transform of the integrand in Eq. (23). The rates were calibrated so that their spatially integrated emission would match the calculated values given in Fig. 3. Figure 9(c) shows the intensities along the diagonals of the calculated images as functions of the in-plane distance from the image center. In both measured and calculated images it is evident that when the QD is close to resonance with the cavity mode, its emission exhibits an in-plane spatial spread that is much larger than the QD size. The closer the emission energy to resonance is the larger is its spatial extent, and vice versa, the larger the detuning is, the more localized the emission pattern becomes. Calculated images, where detuning was modeled by varying the dot size, yielded similar behavior of the emission pattern, implying that the PL spatial spread is mainly a cavity effect depending only on detuning. In general, the calculated images agree with the experimental observations, both in their spatial extent and in their dependence on the detuning, as can be concluded by comparing Fig. 9 with Fig. 8.

A discernible feature in Figs. 8(d) and 9(c) is the dependence of the spacing between the rings in the PL images on the detuning. The rings become more pronounced and denser for increasing positive detuning, where larger $k_\parallel$ are needed for the emission. This gives rise to oscillations that are superimposed on the central emission line due to contributions arising from larger $k_\parallel$ modes. The dependencies of the calcu-

lated locations of the second and third peaks on detuning are shown in Fig. 10(a), and their intensities normalized to the central peak are shown in Fig. 10(b), confirming these observations. Identical results are obtained for both detuning models, suggesting again that this emission pattern is a cavity effect, depending only on detuning. Together with the central peak spread, the locations of the emission rings may aid in evaluating the QD's detuning. We note, though, that as Fig. 10(b) suggests, for spectral lines that are close to resonance with the cavity mode, the relative intensity of the ring emission to the central spot decreases rapidly, making them difficult to measure.

V. SUMMARY

In this paper we have studied the interaction between the electromagnetic modes in a planar cavity and excitons in single QDs embedded at the antinode of the cavity.

We find that the spontaneous emission outside the microcavity is enhanced considerably for dots in resonance with the cavity mode. The emission intensity rapidly decreases with detuning for lines that are positively detuned from the cavity mode. Emission from negatively detuned QDs is largely inhibited, and we were unable to observe any spectral emission below the cavity mode energy. Lifetime measurements have shown a decrease by a factor of roughly 2 for the lifetime of resonant QDs as compared with QDs that are 20 meV detuned from the cavity line. In-plane dispersion of cavity photons was directly observed by strong excitation of

the QD, thereby transforming it into a broadband light source. Finally, we obtained near-field images of the spatial emission distributions from single QDs, showing a large spread over several micrometers in the case of resonant QDs. These images have also shown emission rings with separation and intensity that depend on the detuning of the QD from the cavity mode.

All of these features were qualitatively accounted for by calculations where detuning from the cavity mode was modeled by varying either the QD size or its band gap. For most of the experimental data we have found better agreement with the first mechanism, suggesting that most of the QDs in strain-driven self assembled samples vary in size rather than in composition. The range of $90 \lesssim R_D \lesssim 300$ Å that accounts for the observed phenomena is consistent with typical self-assembled InGaAs/GaAs quantum dots.

ACKNOWLEDGMENTS

APPENDIX

Here we provide some details of the calculation of the exciton's relative motion energy:

$$E_r = \langle \chi_e \chi_h \phi | H_r | \phi \chi_h \chi_e \rangle = 2\pi \mathcal{N}_r^2 (1+\sigma) \frac{\alpha^2}{\eta^{2\alpha}} \int dr \, r^{2\alpha-1}$$

$$\times e^{-2(r/\eta)^\alpha} + k_e^2 \mathcal{N}_{z_e}^2 \left(\sigma_{ez} \frac{L}{2} + \frac{V_e^z}{\kappa_e(k_e^2 + \kappa_e^2)} \right)$$

$$+ k_h^2 \mathcal{N}_{z_h}^2 \left(\sigma_{hz} \frac{L}{2} + \frac{V_h^z}{\kappa_h(k_h^2 + \kappa_h^2)} \right)$$

$$- 4\pi (\mathcal{N}_r \mathcal{N}_{z_e} \mathcal{N}_{z_h})^2 \int dr \, dq \, r J_0(qr) e^{-2(r/\eta)^\alpha} \sum_{i=1}^4 \mathcal{I}_i(q)$$

$$+ \frac{8\pi \mathcal{N}_r^2 \sigma^2}{(1+\sigma)^3 \xi^4} \int dr \, r^3 e^{-2(r/\eta)^\alpha}. \tag{A1}$$

$\mathcal{I}_i(q)$ are given by

$$\mathcal{I}_1(q) = \frac{L}{2q} + \frac{1}{4q^2} \left[\sum_{i=e,h} \frac{g_i}{k_i^2} + \sum_{i \neq j} \frac{g_i}{k_i^2 - k_j^2} \left(\frac{f_j}{q^2 + 4k_e^2} - 1 \right) \right]$$
$$- e^{-qL/2} (f_e - g_e) \frac{\cosh(qL/2)g_h + \sinh(qL/2)f_h}{q^2(q^2+4k_e^2)(q^2+4k_h^2)}, \tag{A2a}$$

$$\mathcal{I}_2(q) = \frac{2k_e^2 e^{-qL/2}}{k_e^2 + \kappa_e^2} \frac{\sinh(qL/2)f_h + \cosh(qL/2)g_h}{q(q+2\kappa_e)(q^2+4k_h^2)}, \tag{A2b}$$

$$\mathcal{I}_3(q) = \frac{2k_h^2 e^{-qL/2}}{k_h^2 + \kappa_h^2} \frac{\sinh(qL/2)f_e + \cosh(qL/2)g_e}{q(q+2\kappa_h)(q^2+4k_e^2)}, \tag{A2c}$$

$$\mathcal{I}_4(q) = \frac{4k_e^2 k_h^2}{(k_e^2 + \kappa_e^2)(k_h^2 + \kappa_h^2)} \frac{\kappa_e + \kappa_h + q}{(\kappa_e + \kappa_h)(2\kappa_e + q)(2\kappa_h + q)}, \tag{A2d}$$

where

$$f_i = 4k_i^2 + q^2 + q^2 \cos(k_i L), \quad g_i = 2qk_i \sin(k_i L). \tag{A3}$$

*Present address: Department of Physics, University of Buffalo, SUNY, Buffalo, NY 15260-1500. Electronic address: guy.ramon@gmail.com

[1] P. Michler, A. Imamoğlu, M. D. Mason, P. J. Carson, G. F. Strouse, and S. K. Buratto, Nature (London) **406**, 968 (2000); C. Santori, M. Pelton, G. Solomon, Y. Dale, and Y. Yamamoto, Phys. Rev. Lett. **86**, 1502 (2001).

[2] D. V. Regelman, U. Mizrahi, D. Gershoni, E. Ehrenfreund, W. V. Schoenfeld, and P. M. Petroff, Phys. Rev. Lett. **87**, 257401 (2001).

[3] A. Kiraz, M. Atatüre, and A. Immamoglu, Phys. Rev. A **69**, 032305 (2004).

[4] E. Knill, R. Laflamme, and G. J. Milburn, Nature (London) **409**, 46 (2001).

[5] C. Santori, D. Fattal, J. Vucković, G. S. Solomon, and Y. Yamamoto, Nature (London) **419**, 594 (2002).

[6] N. Akopian, N. H. Lindner, E. Poem, Y. Berlatzky, J. Avron, D. Gershoni, B. D. Gerardot, and P. M. Petroff, Phys. Rev. Lett. **96**, 130501 (2006).

[7] K. J. Vahala, Nature (London) **424**, 839 (2003).

[8] J. M. Gérard, B. Sermage, B. Gayral, B. Legrand, E. Costard, and V. Thierry-Mieg, Phys. Rev. Lett. **81**, 1110 (1998).

[9] M. Pelton, C. Santori, J. Vucković, B. Zhang, G. S. Solomon, J. Plant, and Y. Yamamoto, Phys. Rev. Lett. **89**, 233602 (2002).

[10] B. Gayral, J. M. Gérard, A. Lemaitre, C. Dupuis, L. Manin, and J. L. Pelouard, Appl. Phys. Lett. **75**, 1908 (1999).

[11] T. Yoshie, A. Scherer, J. Hendrickson, G. Khitrova, H. M. Gibbs, G. Rupper, C. Ell, O. B. Shchekin, and G. Deppe, Nature (London) **432**, 200 (2004).

[12] J. P. Reithmaier, G. Sęk, A. Löffler, C. Hofmann, S. Kuhn, S. Reitzenstein, L. V. Keldysh, V. D. Kulakovskii, T. L. Reinecke, and A. Forchel, Nature (London) **432**, 197 (2004).

[13] A. Badolato, K. Hennessy, M. Atature, J. Dreiser, E. Hu, P. M. Petroff, and A. Imamoglu, Science **308**, 1138 (2005).

[14] L. C. Andreani, G. Panzarini, and J-M. Gérard, Phys. Rev. B **60**, 13276 (1999).

[15] G. Björk, S. Machida, Y. Yamamoto, and K. Igeta, Phys. Rev. A **44**, 669 (1991).

[16] A. J. Bennett, D. C. Unitt, P. See, A. J. Shields, P. Atkinson, K. Cooper, and D. A. Ritchie, Appl. Phys. Lett. **86**, 181102 (2005).

[17] C. Weisbuch, M. Nishioka, A. Ishikawa, and Y. Arakawa, Phys. Rev. Lett. **69**, 3314 (1992).

[18] V. Savona, Z. Hradil, A. Quattropani, and P. Schwendimann, Phys. Rev. B **49**, 8774 (1994).

[19] V. Savona, F. Tassone, C. Piermarocchi, A. Quattropani, and P. Schwendimann, Phys. Rev. B **53**, 13051 (1996).

[20] D. S. Citrin, IEEE J. Quantum Electron. **30**, 997 (1994).

[21] M. Sugawara, J. Appl. Phys. **36**, 2151 (1997).

[22] J. T. Andrews, P. Sen, and R. R. Puri, J. Phys.: Condens. Matter **11**, 6287 (1999).

[23] C. Y. Hu, H. Z. Zheng, J. D. Zhang, H. Zhang, F. H. Yang, and Y. P. Zeng, Appl. Phys. Lett. **82**, 665 (2003).

[24] J. M. Garcia, T. Mankad, P. O. Holtz, P. J. Wellman, and P. M. Petroff, Appl. Phys. Lett. **72**, 3172 (1998).

[25] W. Que, Phys. Rev. B **45**, 11036 (1992).

[26] For a general lateral potential, separation of the c.m. and relative motions is valid only when the QD radius is much larger than the exciton Bohr radius.

[27] M. Sugawara, Phys. Rev. B **51**, 10743 (1995).

[28] R. L. Greene, K. K. Bajaj, and D. E. Phelps, Phys. Rev. B **29**, 1807 (1984).

[29] M. Grundmann and D. Bimberg, Phys. Rev. B **38**, R13486 (1988).

[30] D. Gershoni, C. H. Henry, and G. A. Baraff, IEEE J. Quantum Electron. **29**, 2433 (1993).

[31] J. D. Jackson, *Classical Electrodynamics*, 2nd ed. (John Wiley, New York, 1975).

[32] L. C. Andreani and A. Pasquarello, Phys. Rev. B **42**, 8928 (1990).

[33] E. Dekel, D. Gershoni, E. Ehrenfreund, J. M. Garcia, and P. M. Petroff, Phys. Rev. B **61**, 11009 (2000).

[34] E. Dekel, D. Gershoni, E. Ehrenfreund, D. Spektor, J. M. Garcia, and P. M. Petroff, Phys. Rev. Lett. **80**, 4991 (1998).